Dielectric screening and electric field control of ferromagnetism at the $CaMnO_3/CaRuO_3$ interface

Churna Bhandari* and S. Satpathy
Department of Physics & Astronomy, University of Missouri, Columbia, Missouri 65211, USA

(Received 16 April 2021; revised 7 July 2021; accepted 3 August 2021; published 17 August 2021)

Control of magnetism by an applied electric field is a desirable technique for the functionalization of magnetic materials. Motivated by recent experiments, we study the electric field control of the interfacial magnetism of $CaRuO_3/CaMnO_3$ (CRO/CMO) (001), a prototype interface between a nonmagnetic metal and an antiferromagnetic insulator. Even without the electric field, the interfacial CMO layer acquires a ferromagnetic moment due to a spin-canted state, caused by the Anderson-Hasegawa double exchange (DEX) between the Mn moments and the leaked electrons from the CRO side. An electric field would alter the carrier density at the interface, leading to the possibility of controlling the magnetism, since DEX is sensitive to the carrier density. We study this effect quantitatively using density-functional calculations in the slab geometry. We find a textbook-like dielectric screening of the electric field, which introduces polarization charges at the interfaces and the surfaces. The extra charge at the interface enhances the ferromagnetism via the DEX interaction, while away from the interface the original antiferromagnetic (AFM) state of the Mn layers remains unchanged. The effect could have potential application in spintronics devices.

DOI: 10.1103/PhysRevB.104.085134

I. INTRODUCTION

There is a considerable interest in controlling the magnetism of magnetic materials by an external electric field because of its potential applications in spintronics. Heterostructures between transition metal oxides have been identified as possible platforms for achieving this magnetoelectric coupling effect [1–4]. One such prototypical interface is the (001) interface between the paramagnetic metal $CaRuO_3$ (CRO) and the antiferromagnetic insulator $CaMnO_3$ (CMO), which has been well studied both experimentally and theoretically [4–8]. While CMO is an antiferromagnetic insulator in the bulk, the interface layer adjacent to the paramagnetic CRO acquires a net ferromagnetic moment, while the remaining part of the heterostructure remains unchanged. This has been explained [4,5] to be due to the Anderson-Hasegawa–de Gennes double exchange (DEX) interaction [9–11] between the interfacial Mn magnetic moments and the leaked electrons from the metallic CRO side to the CMO side. The leaked electrons occupy the itinerant Mn-e_g states, which then mediate the DEX interaction between the Mn-t_{2g} core moments, fixed on the lattice sites. The amount of leaked electrons is sufficiently large to produce a spin-canted state in the interfacial MnO layer, resulting in a robust net magnetic moment of about $0.85\mu_B$ per interfacial Mn atom [4].

In the DEX mechanism, the spin canting angle is quite sensitive to the itinerant carrier concentration x, driving the antiferromagnetic (AFM) state into a spin-canted state at first and eventually into an FM state with increasing x. This is apparent from the de Gennes expression [9] for the canting angle, to which we return later, viz., $\theta_c = 2\cos^{-1}(2^{-1}|t|x/J)$, where t is the electron hopping integral and J is the AFM Heisenberg exchange. It is therefore expected that an applied electric field would affect the DEX interaction by modifying the carrier concentration in the magnetic layers. However, the extent of this effect is unknown since dielectric screening theory indicates merely that the polarization charges would accumulate somewhere in the boundary regions, not necessarily in the magnetic layers. Therefore, this issue needs to be studied in detail. Indeed, as our density functional calculations find, much of the surface polarization charges, for example, appear in the vacuum region. It is only the carriers that appear in the magnetic layers that matter as far as the DEX mechanism is concerned.

We chose the prototypical CRO/CMO system for our work since there were already several experimental studies on this system reported in the literature. In fact, Grutter *et al.* [8] recently studied experimentally the electric field dependence of magnetism in this system. They found an increase of the ferromagnetic moment with an applied electric field and concluded that it originated from the interface MnO_2 layer.

In this work, we study the effect of an electric field on the electronic structure and magnetism of the CRO/CMO interface in the slab geometry from density functional calculations. We find a textbook-like dielectric screening of the applied field, which leads to a charge accumulation at the slab surfaces and the interface. However, quite interestingly, not all screening charges occur in the surface or the interface atomic layers. For example, the surface polarization charge is found to occur outside the nominal surface, with little or no charge accumulated on the Mn surface layers or the bulk layers. As for the interfacial Mn layer, a significant amount of extra charge does accumulate there, which reduces the spin

*Current Address: The Ames Laboratory, U.S. Department of Energy, Iowa State University, Ames, IA 50011, USA

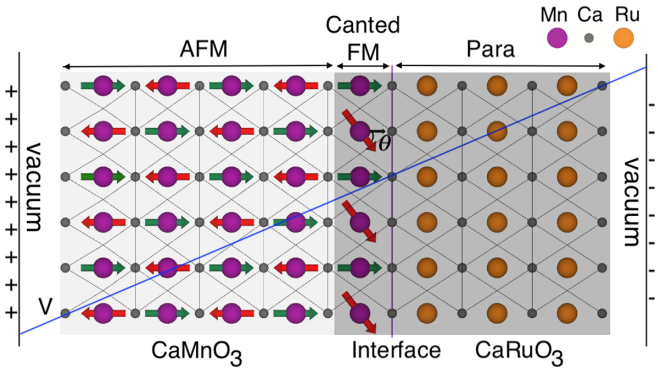

FIG. 1. Schematic diagram of the CMO/CRO heterostructure and the spin-canted state in the interfacial MnO_2 layer. Shown is the supercell used in the DFT calculations along with the electric potential seen by the electrons (blue line) due to the applied electric field. By increasing the charge transfer across the interface, the electric field enhances the interfacial ferromagnetism via double exchange by reducing the canting angle θ. Apart from the enhanced magnetism of the interfacial MnO_2 layer (001) we find that the antiferromagnetism of the remaining CMO layers remain more or less unaffected by the electric field.

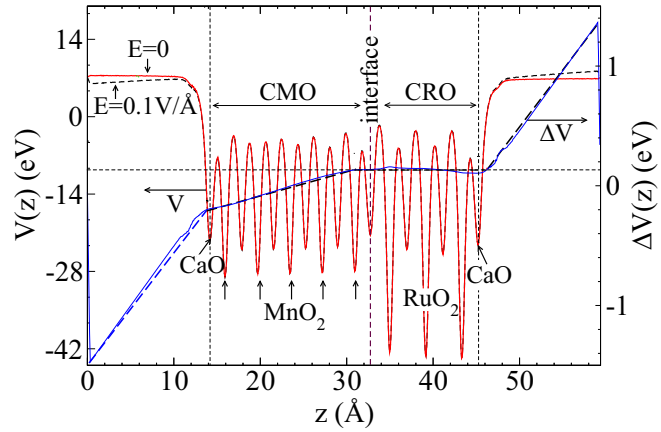

FIG. 2. Planar-averaged potential $V(z)$ seen by the electron both with (red line) and without the electric field (black dashed line). The difference between them ΔV, shown as the blue line, follows a textbook-like linear behavior in each dielectric region as predicted from the dielectric model. The dashed line next to the blue line is a guide to the eye indicating the piecewise linear behavior, the slope of which yields the screened electric field.

canting angle via double exchange when the electric field is applied, leading to an increased net ferromagnetic moment as a result.

II. DENSITY-FUNCTIONAL METHOD

In our calculations, we considered a slab consisting of five layers of CMO and three layers of CRO, $(CMO)_5/(CRO)_3$, with each layer consisting of two formula units to describe the antiferromagnetic Mn moments in CMO. An extra layer of electrically neutral CaO was added as shown in Fig. 1, so that the metal-oxygen octahedra MO_6 is complete on both surfaces. Test calculations using a larger number of layers did not substantially change the results. We used the same in-plane lattice constant as the bulk CMO ($a = 3.73$ Å), while the out-of-plane lattice constant was adjusted to conserve the bulk volume of each constituent material and a vacuum region of 14 Å was added on each side of the slab. Starting from this structure, we relaxed the interlayer distances between all layers. A sawtooth-shaped electrostatic potential was added, as indicated by the dashed line in Fig. 1, which was the supercell we used in the DFT calculations. Dipole correction was included following the work of Bengtsson [12].

The atomic positions were relaxed using the projector augmented wave method (PAW) [13,14] in the generalized gradient approximation (GGA) for the exchange-correlation functional as implemented in the Vienna *ab initio* simulation package (VASP). [15] The QUANTUM ESPRESSO code [16] was used to study the effect of the external electric field on the electronic and magnetic properties, where a norm-conserving ultrasoft pseudopotential was used together with the GGA exchange-correlation functional with the Hubbard parameters $U = 5$ eV and $J = 0$ for the Mn atoms. We used the value of $U = 5$ eV both for the total energy needed for the structural relaxation as well as for the electronic structure including the charge transfer across the interface, while for the magnetic energies listed in Table III, we found $U = 2$ eV to describe the magnetic interactions better.

We note that to obtain good quality results, in the DFT calculations we used a larger field $E = 0.1$ V/Å, than typical experiments. Our results nevertheless establish the two main points of the paper: A quantitative description of the dielectric screening and a semi-quantitative description of the enhancement of the interfacial magnetism due to the charge transfer and double exchange.

III. DIELECTRIC SCREENING CHARGES: MODEL AND DFT RESULTS

The results of our DFT calculations, both with and without an electric field, are shown in Figs. 2 and 3, where we showed the planar averaged Kohn-Sham potential $V(z)$ and the charge density $\rho(z)$, respectively. The planar-averaged quantities are given by the expression $V(z) = A_{\text{cell}}^{-1} \int_{\text{cell}} V(\vec{r}) d^2 r$ and similarly for $\rho(z)$, where the integration is along the plane, normal to the interface, and A_{cell} is the surface cell area. The positions of the individual atomic layers such as MnO_2 can be identified in both figures from the δ-function-like peaks. As seen from Fig. 2, the planar-averaged quantities for with and without the electric field nearly overlap with one another since the differences are very small. The differences, $\Delta V(z)$ and $\Delta\rho(z)$, induced by the electric field are shown as blue lines in Figs. 2 and 3, respectively, on an exaggerated scale.

The DFT results reveal a remarkable textbook-like behavior for the dielectric screening. Points to note are: (i) Piecewise linear potentials in all regions of the slab (Fig. 2), corresponding to the screened electric fields predicted by elementary electrostatics theory (Fig. 4) and (ii) the accumulation of the screening charges at the two surfaces and the interface layer.

A somewhat surprising result is that the screening charges at the two surfaces with the vacuum do not occur on the surface atomic layers as might have been anticipated, but

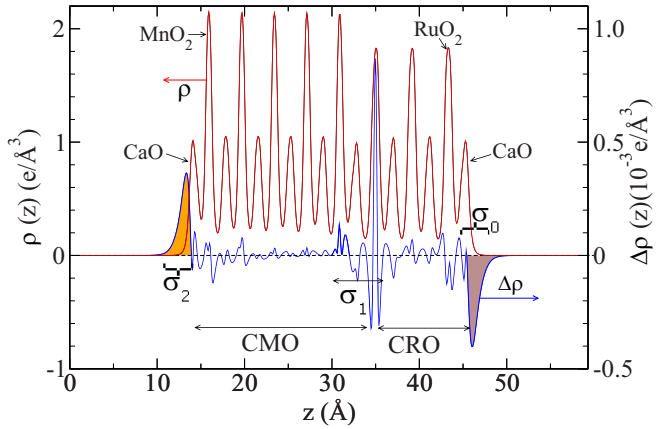

FIG. 3. Planar-averaged electron density for $E = 0$ (red line) and the extra electrons accumulated (polarization charge) (blue line) when the electric field $E = 0.1$ V/ Å is applied. The colored areas under the blue line indicate the net accumulation of charges (positive or negative) at the two surfaces, which are listed in Table I from direct integration.

they rather occur well inside the vacuum region. As seen from Fig. 3, where the polarization charges at the two surfaces have been indicated by colored areas, the polarization charges occur outside the surface CaO layers, at a distance of ∼1.3 Å away from the atomic planes. The screened potential from the DFT calculations (Fig. 2) compares very well with the results of the dielectric screening from elementary electrostatics theory, shown in Fig. 4. The heterostructure is placed between two capacitor plates that produce the electric field E. In the dielectric model, the polarization charges at various boundaries are determined from the Gauss' law, and these are indicated in Fig. 4. Taking κ to be the dielectric constant of the insulator (CMO), the surface charge

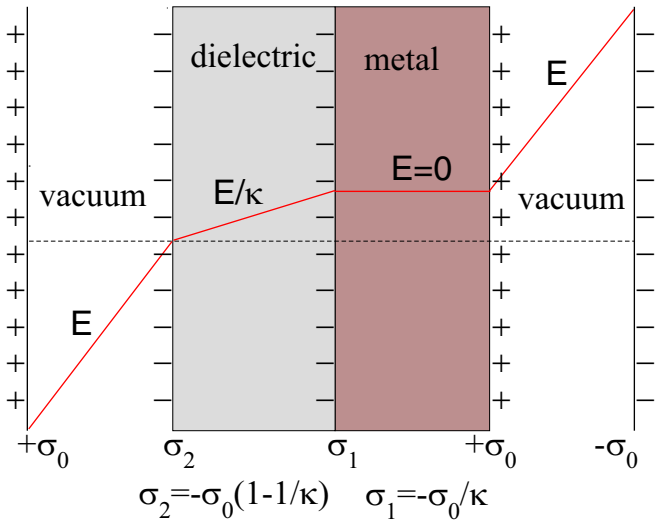

FIG. 4. Polarization charge accumulated at the boundaries for the metal/dielectric slab from elementary electrostatics, relevant for the CMO/CRO film. The slab is placed between two capacitor plates, κ is the relative permittivity of the insulator, and σ_i's indicate the surface charge densities that accumulate at the three boundaries.

TABLE I. Surface polarization charge densities induced by the applied electric field at the interface (σ_1) and the two surfaces (σ_0 and σ_2), computed from the DFT as well as from the electrostatics theory. The applied electric field is $E = 0.1$ V/Å, the relative permittivity $\kappa = 5$ is used in the dielectric model, and the surface charge densities are expressed in units of $10^{-4}|e|/\text{Å}^2$.

	σ_0	σ_1	σ_2
DFT	5.4	−1.1	−4.3
Dielectric model	5.53	−1.11	−4.42

densities are: $\sigma_0 = -\epsilon_0 E$ at the metal surface, where ϵ_0 is the vacuum permittivity, $\sigma_1 = -\sigma_0/\kappa$ is the charge density at the interface between the metal and the dielectric, and $\sigma_2 = -\sigma_0(1 - 1/\kappa)$ is the charge density at the surface dielectric surface. Taking the value $\kappa \approx 5$ to fit with our DFT results for the screening charges and the vacuum permittivity $\epsilon_0 = 8.85 \times 10^{-12} F/m = 5.53 \times 10^{-3}|e|/$ (V/Å), for the case $E = 0.1$ eV/Å, we get the numerical values: $\sigma_0 = 5.53$, $\sigma_1 = -1.11$, and $\sigma_2 = -4.42$, in units of 10^{-4} $|e|/\text{Å}^2$. These values together with the corresponding DFT results are listed in Table I.

The DFT values were computed by integrating the planar averaged charge difference $\Delta\rho$ near the CRO and CMO surfaces indicated by the colored areas in Fig. 3. The computed values are $\sigma_0^{\text{DFT}} = 5.4 \times 10^{-4}$ $|e|/\text{Å}^2$ and $\sigma_2^{\text{DFT}} = -4.3 \times 10^{-4}$ $|e|/\text{Å}^2$. Since the interface charge σ_1 is relatively smaller and charges fluctuate quite a bit near the CMO/CRO interface, we were not able to get the value of σ_1 reliably by direct integration. Instead, we obtained σ_1 from the charge neutrality condition, viz., $\sum_{i=1}^{3} \sigma_i = 0$, using the integrated values for σ_0 and σ_2, with the result $\sigma_1^{\text{DFT}} = -1.1 \times 10^{-4}$ $|e|/\text{Å}^2$. All these values agreed quite well with the polarization charges obtained from the dielectric model (Table I), assuming the dielectric constant to be $\kappa \approx 5$. In comparison to this, the corresponding experimental value $\kappa \approx 7$, inferred from the optical conductivity data [17], is somewhat larger. The reason for this difference could be due to the approximate nature of the functionals used in the DFT calculations or due to the small number of layers in the supercell used, so that the bulk dielectric screening limit has not been reached.

As seen from Figs. 2 and 4 and Table I, the DFT results agree quite well with the textbook-like screening profile including the screened electric fields and the polarization charges at the boundaries. Figure 2 shows that the final screened electric fields in various regions are uniform (linear ΔV) as expected from the electrostatics model. While in the vacuum region, the applied electric field is unchanged, it is completely screened in the metallic region (CRO) as expected ($\kappa = \infty$) and is reduced by the dielectric constant κ in the insulating region (CMO). Taking the ratio of the screened electric field in the CMO region to the applied electric field (Fig. 2), we get a second estimate $\kappa \approx 4.4$, which is similar to the value $\kappa \approx 5$ obtained from the surface polarization charges discussed above.

As already mentioned, we find that the polarization charges do not necessarily reside on the atomic layers. For our purpose, it is important to study the electronic charges on the

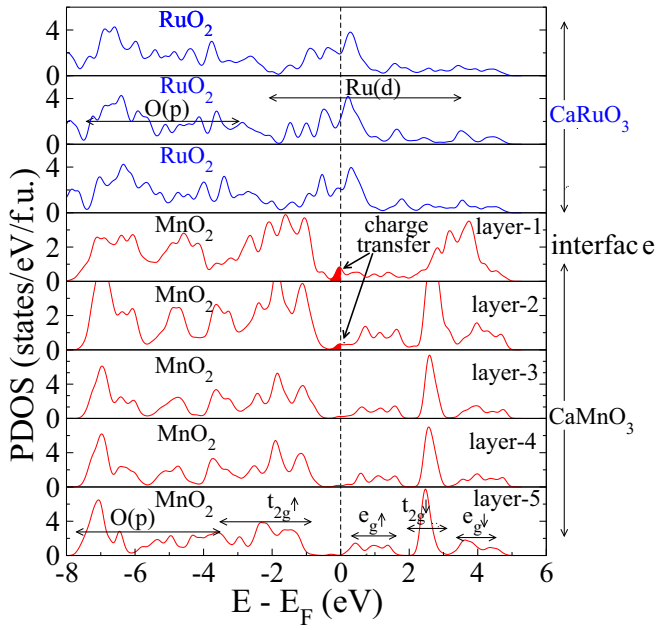

FIG. 5. Partial densities of states (PDOS) for Mn and Ru layers in units of states/eV/ formula unit (MnO_2 or RuO_2) including both spins. Charge transfer across the interface to the CMO side (primarily Mn-e_g states) are indicated by two arrows in the middle two panels. Here, the electric field is $E = 0$. With the applied electric field, the figure remains more or less the same except that the charge transfer to the CMO side is a bit larger as listed in Table II.

individual atomic layers, especially the Mn layers, as the itinerant Mn-e_g electrons mediate the DEX between the core t_{2g} spins leading to spin canting. For this purpose, we computed the layer-resolved partial density of states (PDOS) on the individual MnO_2 and RuO_2 layers, which are shown in Fig. 5. In the CMO bulk, the material is an insulator with filled majority-spin t_{2g} bands and empty e_g bands, as indicated in the bottom panel of Fig. 5. There is some charge transfer across the interface from the RuO side to the two neighboring MnO_2 layers as indicated in the figure. By directly integrating the area of the occupied Mn-e_g states (marked in red in Fig. 5), we can compute the charge transfer into various MnO_2 layers in the structure. There is significant charge transfer only to the first two MnO_2 layers at the interface as indicated in Fig. 5.

The charge transfer to the various MnO_2 layers from the RuO side are also listed in Table II. Without the electric field, there is already a charge transfer from the CRO side to the CMO side [5]. This leads to a net dipole moment with a positive charge on the CRO side and a negative charge on the CMO side, but there is no net monopole charge. As seen from Table II, for $E = 0$, the charge accumulated on the first MnO_2 layer is 0.117 e^-/Mn atom $\approx 8.4 \times 10^{-3}$ $e^-/\text{Å}^2$. The accumulated electrons occupy the Mn e_g states, serving as the itinerant electrons that mediate the double exchange between the Mn t_{2g} core spins, which we discuss in more detail in Sec. IV.

When the electric field is applied, there are monopole charges σ_i that accumulate at various boundaries to screen out the applied field. These add to the layer charges already existing for $E = 0$. Table II shows that with $E = 0.1$ V/Å, the first MnO_2 layer gains a small additional charge making the total in that layer to be 0.121 e^-/Mn atom, which translates into an additional charge of 0.004 e^-/Mn atom (-2.9×10^{-4} $|e|/\text{Å}^2$). Note that, although it is of the same order of magnitude as the interface polarization charge σ_1 seen from Table II, they are not necessarily the same, as σ_1 is not necessarily located entirely on the interfacial MnO_2 layer. For the DEX interaction on the interfacial MnO layer, it is only the net charge (itinerant e_g electrons) on that layer that matters, not the total polarization charge that accumulates in the interface region due to the dielectric screening. As seen from Fig. 3, the polarization charge σ_1 is spread over several monolayers at the interface region, both on the CMO and the CRO sides.

As we move away from the interface, the accumulated charge in the MnO_2 layers quickly reverts to the bulk value as seen from Table II. The bulk limit is already reached as quickly as the third layer and beyond. An interesting point to note regarding the surface charges at the vacuum interface is that even though there is a considerable polarization charge ($\sigma_2 = -4.3 \times 10^{-4}|e|/\text{Å}^2$ at the CMO/vacuum interface from Table I), only a small fraction of it appears on the surface MnO_2 layer (layer-5 in Table II). Indeed as observed already, much of the charge of both σ_2 and σ_0 at the two surfaces appear well inside the vacuum region, with the peaks appearing about 1.3 Å outside of the terminal CaO surface. Thus, the surface MnO_2 layer being more or less similar to the bulk, with very little additional charge transfer due to the electric field, the magnetism continues to remain antiferromagnetic, i.e., the same as in the bulk. This is also confirmed from the total energy calculations within the DFT, which shows the MnO_2 surface layer to remain antiferromagnetic.

TABLE II. Extra electrons per Mn atom, as compared to the bulk, accumulated at various MnO_2 layers near the interface. The electrons occupy the Mn e_g states as indicated from Fig. 5. Electric field E is in units of (V/Å). These numbers are to be multiplied with the factor 7.2×10^{-2} to get the electron numbers in units of $e^-/\text{Å}^2$ for the corresponding MnO layer for comparison with the polarization charges shown in Table I.

E	layer-1	layer-2	layer-3	layer-4	layer-5
0	0.117	0.044	0.002	0.000	0.000
0.1	0.121	0.045	0.002	0.001	0.002

IV. SPIN CANTING AND INTERFACIAL FERROMAGNETISM

A. Ferromagnetism at the interface

To study the stability of the interfacial magnetism, we computed the total energy of the two magnetic structures, one where all Mn atoms are antiferromagnetic (AFM) as in the bulk and a second structure, where only the interfacial MnO_2 layer is ferromagnetic (FM), while the remaining layers retain the AFM structure of the bulk. We find that even though the energy difference between the FM and AFM configurations for the Mn–Mn bond at the interface is somewhat sensitive

TABLE III. Calculated total energy, where the CMO layer at the interface is either FM or AFM, with the remaining layers being AFM, i.e., the same as in the bulk. Energies are per interfacial bond and in units of meV for the electric fields $E = 0$ and $E = 0.1$ V/Å.

E	FM	AFM
0	−16.1	0
0.1	−19.2	0

to the magnitude of the Coulomb repulsion parameter U used in the DFT calculations, the FM state is always more stable. In Table III, we list the results for $U = 2$ eV, for which the computed $\Delta E \equiv E_{\uparrow\downarrow} - E_{\uparrow\uparrow} = 16.1$ meV value for $E = 0$ is comparable to the experimental value of 13.1 meV for the bulk CMO [18,19]. As seen from Table III, the FM state is further stabilized under the applied electric field by about 3 meV for $U = 2$ eV. If we use the value $U = 5$ eV, this extra stabilization energy is about 2 meV. The other quantities such as the charge transfer and the density of states are not sensitive to the value of U, and were calculated with $U = 5$ eV.

Table III shows that the FM state of the interfacial MnO_2 layer is more stable both with and without the external electric field. As discussed later, the spin-canted state, which has a reduced net FM moment, has actually even lower energy than the FM state, which has been confirmed earlier for the intrinsic sample ($E = 0$) both from the experiment and theory [4,5]. With the application of the electric field, the total energy of the FM state is further reduced by about 3 meV, making the FM state even more stable in the presence of an electric field. As already mentioned, we also computed the same energy difference for the surface MnO_2 layer and find that, in contrast to the interfacial MnO_2 layer, the AFM state at the surface continues to remain energetically favorable, both with and without the electric field.

These results are consistent with the Anderson-Hasegawa DEX result that the FM state becomes progressively more energetically favored over the AFM state as the itinerant carrier concentration is increased, in our case by the application of the electric field. However, the lowest-energy state is neither FM nor AFM, but a spin-canted state, and we discuss this by considering a simple DEX model on a square lattice that describes the magnetism of the interfacial MnO_2 layer.

B. Double-exchange model and spin canting

We consider the well-known Anderson-Hasegawa double exchange model [9–11,20] and apply it to a square lattice appropriate for the MnO_2 layer. The Hamiltonian is

$$\mathcal{H} = t \sum_{\langle ij\rangle\sigma} c^{\dagger}_{i\sigma} c_{j\sigma} + \text{H.c.} + \sum_{\langle ij\rangle} J\hat{S}_i \cdot \hat{S}_j - 2J_H \sum_i \vec{S}_i \cdot \vec{s}_i, \tag{1}$$

which describes the motion of the itinerant Mn (e_g) electrons (the corresponding field operators are $c^{\dagger}_{i\sigma}, c_{j\sigma}$ with i and σ being the site and the spin indices) moving in a lattice of Mn t_{2g} core spins ($S = 3/2$). Here t is the tight-binding nearest-neighbor hopping, $\mathbf{s}_i = 1/2 \sum_{\mu\nu} c^{\dagger}_{j\mu} \tau_{\mu\nu} c_{j\nu}$ is the spin of the itinerant electron with the Pauli matrices τ, J is the superexchange, J_H is the Hund's coupling, and the angular brackets indicate sum over distinct pairs of bonds in the lattice. Typical parameters for CMO are [5,21] $t = -0.15$ eV, $J = 7$ meV, and $J_H = 0.85$ eV.

It is instructive to consider the de Gennes result [9] for the limiting case $J_H = \infty$, which suggests a spin-canted state in the presence of the itinerant carriers. In this limit, since only one spin channel parallel to the core spins is available for the itinerant electrons, Eq. (1) is equivalent to the spinless Hamiltonian $\mathcal{H} = \sum_{\langle ij\rangle} t \cos(\theta_{ij}/2)\, c^{\dagger}_i c_j + \text{H.c.} + \sum_{\langle ij\rangle} J\hat{S}_i \cdot \hat{S}_j$, where the hopping has been modified by the well-known Anderson cosine factor [10], with θ_{ij} being the polar angle difference between the neighboring core spins. Taking a bipartite square lattice, with the spins in the two sublattices (A and B) canted by the angle θ with respect to one another, and considering a small concentration x of the itinerant carriers, the electrons occupy the band bottom $E_b = -z|t|\cos(\theta/2)$, where $z = 4$ is the number of nearest neighbors. The canting angle θ_c is obtained by minimizing the total energy

$$E = E_b x + (z/2)J\cos\theta, \tag{2}$$

which yields the result

$$\theta_c = 2\cos^{-1}\left(\frac{|t|x}{2J}\right). \tag{3}$$

For the $J_H =$ finite case, no such analytical result is possible, and we must solve for the band-structure energies ε_{nk} by keeping both spin channels in the Hamiltonian (1) and sum over the occupied states. The canting angle θ_c is obtained by numerical minimization of the total energy

$$E = (z/2)J\cos\theta + \sum_{nk}^{\text{occ}} \varepsilon_{nk}. \tag{4}$$

The computed total energy is shown in Fig. 6(a) as a function of the canting angle θ for various electron concentration x. As seen from the figure, when the electron concentration $x = 0$, the minimum energy occurs at the canting angle $\theta_c = \pi$ resulting in an AFM state, obviously due to the super exchange interaction J, which is the only interaction without any itinerant carriers. With increasing x, the strength of the DEX interaction slowly increases, producing a spin-canted state, and eventually, beyond a critical value $x > x_c$, the DEX dominates resulting in an FM state ($\theta_c = 0$).

The critical concentration in the $J_H = \infty$ limit is given by Eq. (3) and has the value $x_c = 2J/|t| \approx 0.09\ |e|/$ interfacial Mn atom, which is also seen from Fig. 6(b), where we present the concentration dependence of the canting angle for several values of J_H. It is clear that for $J_H = 0$, the itinerant and the core spins are not coupled and therefore the system remains AFM for all x due to the super exchange interaction of the core spins, up to the full occupation of the bands. As J_H is increased from zero, the critical concentration x_c monotonically decreases, eventually approaching the de Gennes result $x_c = 2J/|t|$ for $J_H = \infty$. The critical values of x_c shown in Fig. 6(b) for the three values of J_H are consistent with this expectation.

We now discuss the effect of the electric field on the charge transfer across the interface into the MnO_2 layer, which in turn affects the spin canting and therefore the net ferromagnetism. As seen from Table II, there is already a significant charge

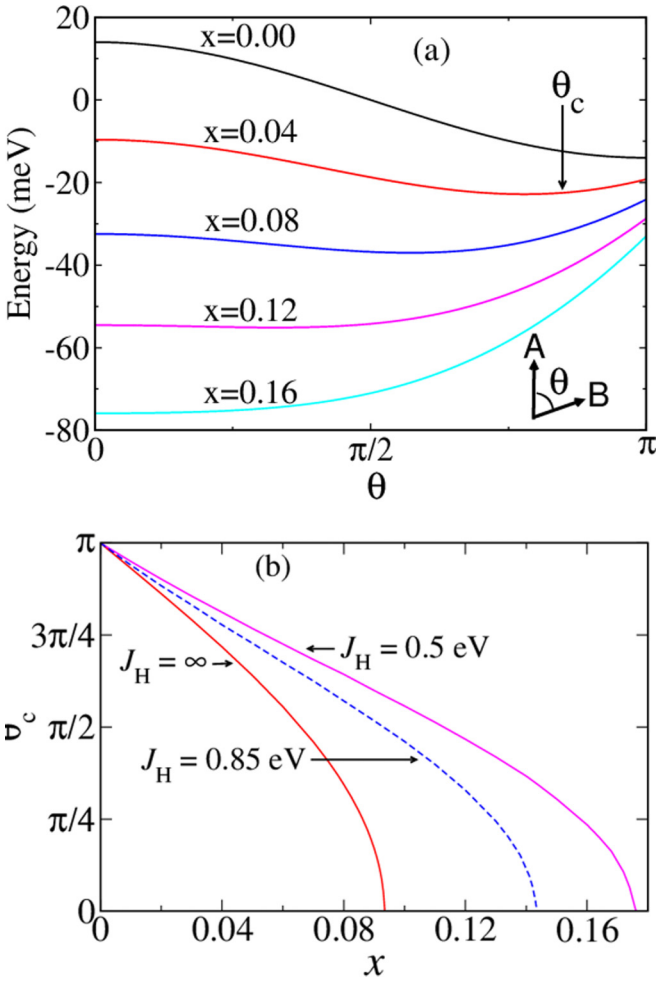

FIG. 6. Energetics of the spin-canted state. (a) Energy from Eq. (4) as a function of the angle θ between spins in the two sublattices, A and B, for several values of the electron concentration x. The minimum yields the canting angle θ_c (indicated by an arrow for the $x = 0.04$ case). Starting from the AFM state ($\theta_c = \pi$) for $x = 0$, the system turns into an FM state ($\theta_c = 0$) beyond the critical concentration $x_c \approx 0.135$, so that one obtains an FM state for the case $x = 0.16$. The parameters are $J = 7$ meV, $t = -0.15$ eV, and $J_H = 0.85$ eV. (b) The spin canting angle θ_c as a function x for three cases: $J_H = 0.5$ eV, 0.85 eV, and ∞, with the parameters J and t being the same as in panel (a). The critical concentration x_c, beyond which an FM state is obtained ($\theta_c = 0$), is where the curves meet the x axis. With increasing x, θ_c decreases, leading to an enhancement of the net ferromagnetic moment.

leakage to the interfacial MnO_2 layer even for $E = 0$, which leads to a canted AFM state. The magnitude of the canting angle θ_c can be estimated from Fig. 6(b). With the applied electric field, the charge transfer increases due to the build up of the dielectric screening charges. As a result, the canting angle decreases, thereby leading to the enhancement of the net FM moment. The net FM moment per Mn atom in the MnO_2 layer is given by the expression $m = m_s(1 + \cos\theta_c)/2$, where $m_s \approx 3\ \mu_B$ is the Mn core spin moment.

If we take $J_H \approx 0.85$ eV for CMO [21], the cant angle θ_c decreases from 66.4° to 57.8°, the predicted increase obtained from Fig. 6(b) is from $m = 2.1\ \mu_B$ ($E = 0$) to $2.3\ \mu_B$ ($E = 0.1$ V/Å), corresponding to the change in the electron concentration of $x = 0.117$ to 0.12 electron/Mn atom, as seen from Table II.

Indeed, such an enhancement of the net FM moment has been observed in the neutron reflectivity experiments [8]. However, the experiment shows a much larger increase in the FM moment, viz., from 1 μ_B to 2.5–3.0 μ_B, corresponding to the transition from a canted AFM state to a fully FM state of the Mn^{+4} ion at the interface. However, notice from Fig. 6(b) that the canting angle is quite sensitive to the itinerant carrier concentration x in the interfacial MnO_2 layer, and a critical value of $x_c \approx 0.14$ (for $J_H = 0.85$ eV) would turn the system completely ferromagnetic. This reflects an increase of the itinerant carriers by just 0.02 $|e|$/ Mn atom by the electric field on top of the $\sim$0.12$|e|$/ Mn atom that already exists in the intrinsic interface for $E = 0$.

Even though the theory and experiments agree qualitatively on the increase of the FM moment with the electric field, a quantitative comparison is difficult owing to several factors. One, it is difficult to experimentally determine the exact magnitude of the electric field that is applied to the CRO/CMO heterostructure since the structure is capped by several other layers of materials in the actual sample [22]. Second, transition-metal oxide samples are notorious for the oxygen stoichiometry issues and it is quite conceivable that the applied electric field leads to a migration of the oxygen atoms to the interface, leading to an extra mechanism of charge accumulation at the interface. Since the double exchange mechanism becomes stronger with an increase of the carrier concentration x, this would increase the tendency towards ferromagnetism, and as already pointed out just an extra 0.02 $|e|$/Mn atom at the interface is needed to drive the system completely ferromagnetic. Finally, there may be substrate-induced strain in the interface, which was not studied in the experiment, nor was it considered in our theory. Test calculations for a strained structure corresponding to the in-plane lattice constant of the $SrTiO_3$ substrate ($\approx$4.8% tensile strain for CMO) indicated a slight increase on the charge transfer to the first interfacial CMO layer, from 0.117 to 0.120 e^- per Mn atom, which would somewhat increase the ferromagnetic moment due to a reduction in the spin-canting angle. It would be desirable to study these effects further.

V. SUMMARY

In summary, we studied the effect of an external electric field on the CRO/CMO (001) interface using density functional methods to understand the field tuning of the magnetism at the interface. This system was chosen due to the existing experiments, but the conclusions should be valid for a variety of interfaces.

We found several interesting results. (1) The polarization charges induced at the interface and the surfaces with the vacuum to screen the applied electric field followed a textbook-like profile. (2) Interestingly, the surface polarization charges occurred well inside the vacuum (at a distance of about 1.3 Å from the surface atomic planes). Similarly, the interface polarization charge is spread over several atomic planes in the interface region, which means that not necessarily all of it participate in the interface phenomena such

as the double exchange in our case. (3) The surface MnO_2 layer is predicted to remain AFM as in the bulk, so that the enhancement in the ferromagnetism seen in the experiments is unlikely to come from the surface, as has been suggested in the experiments [8]. (4) Our theoretical work supports the experimental observation that the interfacial magnetism is enhanced by the applied field and identifies the extra charge accumulation at the interface MnO_2 layer and the double exchange mechanism to be responsible for the enhancement. However, the effect is much stronger experimentally than the theory predicts. The difficulty of a quantitative comparison with the experiment is due to several factors, viz., (i) the possibility of electric-field driven oxygen migration to the interface, (ii) the unknown magnitude of the electric field at the interface due to the presence of the substrate and the cap layers in the experiments, and (iii) the possible strain in the structure due to the substrate. Nevertheless, both the theory and experiment indicate a strong electric field tuning of the interfacial magnetism, with potential for application in magnetoelectric devices.

ACKNOWLEDGMENTS

We thank Professor Yuri Suzuki for stimulating this work and for her insightful discussions. We acknowledge financial support from the US Department of Energy, Office of Basic Energy Sciences, Division of Materials Sciences and Engineering Grant No. DE-FG02-00ER45818. Computational resources were provided by the National Energy Research Scientific Computing Center, a user facility also supported by the US Department of Energy.

[1] K. Ueda, T. Hitoshi, and T. Kawai, Ferromagnetism in $LaFeO_3$-$LaCrO_3$ superlattices, Science **280**, 1064 (1998).

[2] M. Gibert, P. Zubko, R. Scherwitzl, J. Íñiguez, and J.-M. Triscone, Exchange bias in $LaNiO_3 - LaMnO_3$ superlattices, Nat. Mater. **11**, 195 (2012).

[3] A. J. Grutter, H. Yang, B. J. Kirby, M. R. Fitzsimmons, J. A. Aguiar, N. D. Browning, C. A. Jenkins, E. Arenholz, V. V. Mehta, U. S. Alaan, and Y. Suzuki, Interfacial Ferromagnetism in $LaNiO_3/CaMnO_3$ Superlattices, Phys. Rev. Lett. **111**, 087202 (2013).

[4] K. S. Takahashi, M. Kawasaki, and Y. Tokura, Interface ferromagnetism in oxide superlattices of $CaMnO_3/CaRuO_3$, Appl. Phys. Lett. **79**, 1324 (2001).

[5] B. R. K. Nanda, S. Satpathy, and M. S. Springborg, Electron Leakage and Double-Exchange Ferromagnetism at the Interface Between a Metal and an Antiferromagnetic Insulator: $CaRuO_3/CaMnO_3$, Phys. Rev. Lett. **98**, 216804 (2007).

[6] J. W. Freeland, J. Chakhalian, A. V. Boris, J.-M. Tonnerre, J. J. Kavich, P. Yordanov, S. Grenier, P. Zschack, E. Karapetrova, P. Popovich, H. N. Lee, and B. Keimer, Charge transport and magnetization profile at the interface between the correlated metal $CaRuO_3$ and the antiferromagnetic insulator $CaMnO_3$, Phys. Rev. B **81**, 094414 (2010).

[7] C. He, A. J. Grutter, M. Gu, N. D. Browning, Y. Takamura, B. J. Kirby, J. A. Borchers, J. W. Kim, M. R. Fitzsimmons, X. Zhai, V. V. Mehta, F. J. Wong, and Y. Suzuki, Interfacial Ferromagnetism and Exchange Bias in $CaRuO_3/CaMnO_3$ Superlattices, Phys. Rev. Lett. **109**, 197202 (2012).

[8] A. J. Grutter, B. J. Kirby, M. T. Gray, C. L. Flint, U. S. Alaan, Y. Suzuki, and J. A. Brochers, Electric Field Control of Interfacial Ferromagnetism in $CaMnO_3/CaRuO_3$ Heterostructures, Phys. Rev. Lett. **115**, 047601 (2015).

[9] P.-G. De Gennes, Effects of double exchange in magnetic crystals, Phys. Rev. **118**, 141 (1960).

[10] P. W. Anderson and H. Hasegawa, Considerations on double exchange, Phys. Rev. **100**, 675 (1955).

[11] C. Zener, Interaction between the d-shells in the transition metals. II. Ferromagnetic compounds of manganese with perovskite structure, Phys. Rev. **82**, 403 (1951).

[12] L. Bengtsson, Dipole correction for surface supercell calculations, Phys. Rev. B **59**, 12301 (1999).

[13] P. E. Blöchl, Projector augmented-wave method, Phys. Rev. B **50**, 17953 (1994).

[14] G. Kresse and D. Joubert, From ultrasoft pseudopotentials to the projector augmented-wave method, Phys. Rev. B **59**, 1758 (1999).

[15] G. Kresse and J. Furthmüller, Efficient iterative schemes for *ab initio* total-energy calculations using a plane-wave basis set, Phys. Rev. B **54**, 11169 (1996).

[16] P. Giannozzi, S. Baroni, N. Bonini, M. Calandra, R. Car, C. Cavazzoni, D. Ceresoli, G. L. Chiarotti, M. Cococcioni, I. Dabo *et al.*, J. Phys.: Condens. Matter **21**, 395502 (2009); **29**, 465901 (2017).

[17] N. N. Loshkareva, L. V. Nomerovannaya, E. V. Mostovshchikova, A. A. Makhnev, Yu. P. Sukhorukov, N. I. Solin, T. I. Arbuzova, S. V. Naumov, N. V. Kostromitina, A. M. Balbashov, and L. N. Rybina, Electronic structure and polarons in $CaMnO_{3-\delta}$ single crystals: Optical data, Phys. Rev. B **70**, 224406 (2004).

[18] E. O. Wollan and W. C. Koehler, Neutron diffraction study of the magnetic properties of the series of perovskite-type compounds $[(1-x)\mathrm{La}, x\mathrm{Ca}]MnO_3$, Phys. Rev. **100**, 545 (1955).

[19] H. Meskine, H. König, and S. Satpathy, Orbital ordering and exchange interaction in the manganites, Phys. Rev. B **64**, 094433 (2001).

[20] S. K. Mishra, S. Satpathy, F. Aryasetiawan, and O. Gunnarsson, Possible suppression of canted spin order in the double-exchange lanthanum manganites, Phys. Rev. B **55**, 2725 (1997).

[21] S. Satpathy, Z. S. Popović, and F. R. Vukajlovic, Electronic Structure of $La_{1-x}Ca_xMnO_3$, Phys. Rev. Lett. **76**, 960 (1996).

[22] Y. Suzuki, private communications.